Lab on a Chip

ROYAL SOCIETY OF CHEMISTRY

PAPER

View Article Online
View Journal | View Issue

Check for updates

Cite this: *Lab Chip*, 2026, **26**, 2709

Integration of continuous microfluidic electrokinetic bioparticle preconcentration with programmable extraction into a discrete microfluidic platform

Amir Hillman, [a] Sinwook Park[a] and Gilad Yossifon *[ab]

Received 27th June 2025,
Accepted 6th March 2026

DOI: 10.1039/d5lc00647c

rsc.li/loc

This study presents a hybrid platform that integrates continuous and digital microfluidics (DMF) to generate preconcentrated discrete droplets from ionic concentration-polarization (ICP) based preconcentration occurring within a continuous medium. This study expands previous work on droplet generation using electrowetting-on-dielectric (EWOD)-based DMF, transitioning from continuous flow in a microchannel to incorporating electrokinetic molecule preconcentration, followed by the extraction of the molecules into droplets in air, without the need for an oil phase, while effectively maintaining their molecular preconcentrated state. Experiments were complemented with numerical simulations and an analytical model, showing qualitative agreement.

Introduction

Ion-exchange membranes exhibit selective ion transport, allowing counterions to traverse the membrane while effectively blocking co-ions. This selective permeability leads to the phenomenon known as ion concentration polarization (ICP) under the influence of an electric current, creating regions of ion enrichment and depletion at the interfaces between the membrane and the electrolyte. At the boundary of the depletion zone, where steep conductivity gradients are present, a dynamic equilibrium forms between convective transport and electromigration, especially for species such as bioparticles that are present at lower concentrations than the bulk electrolyte. This mechanism enables continuous preconcentration of such analytes.[1–4] ICP-based techniques significantly improve the sensitivity of bioparticle detection in microscale bioanalytical systems.[5–8] A common method involves using two ion-permselective membranes in series, applying opposite electrical potentials to establish an ionic concentration gradient to localize the preconcentrated plug.[9,10] ICP-based preconcentration faces a limitation in that it requires continuous flow and voltage to maintain the preconcentrated plug, which hinders its extraction for further processing.[9] Therefore, an efficient method is needed to extract the plug from ICP-based devices.[11,12]

Digital microfluidics (DMF) systems precisely manipulate liquid droplets by independently addressing them on an electrode array, typically in air or oil.[13] Droplets are controlled between two slides with electrodes coated in dielectric and hydrophobic layers, and are typically powered by AC voltage to prevent electrolysis.[14,15] DMF enables droplet merging, mixing, splitting, and extraction from reservoirs, making it valuable for lab-on-a-chip assays involving bioparticles.[13] Numerous studies have demonstrated its effectiveness in cell manipulation,[16] sample introduction to biosensors,[17,18] and various DNA processing assays.[19,20] In summary, DMF provides an efficient approach for handling liquid droplets in biological lab-on-a-chip applications.

Ongoing research seeks to combine the advantages of continuous and discrete microfluidics by developing hybrid platforms. One approach uses a DMF platform in which consecutive electrodes draw liquid, creating a fully wetted array that mimics continuous microfluidics.[21–23] However, such platforms lack the ability to perform true continuous flow operations, as the fully wetted array atop the electrodes remains stationary. Another strategy integrates a continuous microchannel with a DMF electrode array directly, on a single device.[24] Nevertheless, in this design, the microchannel terminates directly at the DMF electrodes, preventing continuous-flow sample manipulations, such as ICP-based molecular and bioparticle preconcentration, that require sustained flow preceding droplet generation. Other integrated systems bridge droplet microfluidics and DMF *via* a capillary tube, but rely on an oil phase for droplet encapsulation, which limits further processing.[25,26] Similarly, other systems

---

[a] *School of Mechanical Engineering, Tel-Aviv University, Israel. E-mail: gyossifon@tauex.tau.ac.il*
[b] *School of Biomedical Engineering, Tel-Aviv University, Israel*

utilize an oil phase to generate ICP-based preconcentrated droplets, but lack integration with DMF.[27,28] Additional hybrid platforms transport discrete droplets onto a DMF electrode array and introduce them to a microchannel inlet. However, they can only fill microchannels and cannot generate discrete droplets from continuous flows.[29–31] Therefore, there is a critical need for a hybrid platform that seamlessly integrates continuous-flow microfluidics with DMF to directly generate discrete droplets from single-phase microchannels.

While numerous continuous microfluidic techniques exist for manipulating bioparticles, a significant challenge remains in extracting these preconcentrated species, such as DNA, proteins, exosomes, and cells, from the microfluidic system for further processing.[7,8,32] These particles are typically preconcentrated *in situ* within the microchannel, and attempts to relocate them often result in diffusive or convective mixing and smearing, thereby compromising their concentrated state.[9,11,12] The extraction of concentrated droplets offers significant advantages for microfluidic workflows, such as reducing bioassay completion times,[33] and encapsulating preconcentrated biomarkers that are otherwise scarce in their native samples for downstream detection or reaction.[12,28,34] Direct transfer of these enriched droplets onto a DMF platform establishes a seamless interface between continuous microfluidics-based molecular and bioparticle preconcentration and droplet-based processing. This integration leverages the inherent advantages of DMF for programmable droplet manipulation, enabling the execution of multistep bioassays on a single, streamlined lab-on-a-chip platform that combines the strengths of continuous microfluidics and DMF-based sample processing and fluid handling. This study investigates the conditions required to extract a controlled volume of liquid from a microchannel onto a DMF platform while preserving the preconcentrated state of molecules achieved *via* ICP in the main microfluidic channel. This is enabled by an interfacing microfluidic region filled with stagnant liquid, positioned between the continuously flowing main microchannel and the DMF platform, allowing on-demand extraction of concentrated species into discrete droplets in air with defined volume and biomolecule concentration.

Materials and methods

Experimental setup

We designed and fabricated a hybrid platform that integrates continuous microfluidics with EWOD-based DMF to generate ICP-preconcentrated droplets, as illustrated in Fig. 1. The platform consists of a main microchannel intersected by a side microchannel, with a pair of Nafion ion-selective membranes positioned upstream and downstream of the intersection. Both the main and side microchannels are 600 μm wide and 25 μm high. The side microchannel terminated

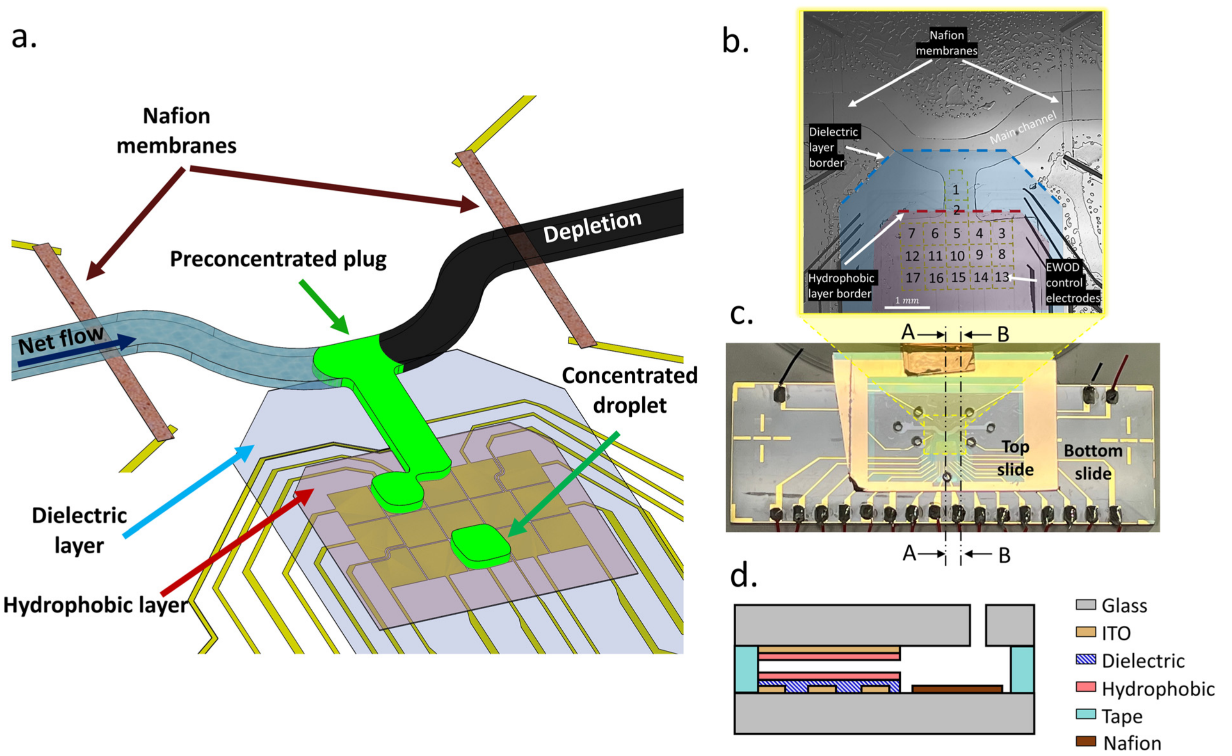

Fig. 1 Platform configuration. (a) Schematic illustration of utilization of ion concentration-polarization within the microchannel and the subsequent generation of concentrated droplets using EWOD. (b) Components of the fabricated chip with a detailed view of the microchannel–EWOD interface. (c) Image of the overall fabricated chip. (d) Side view schematic (not to scale) of the platform, combining the layers shown in cross-sections A–A and B–B, illustrating its different layers and components.

at a hydrophobic barrier, covering both electrode #1 and a portion of electrode #2 (Fig. 1), and interfaced with a 3 × 5 array of square DMF electrodes, each measuring 500 × 500 μm. The DMF electrodes were fabricated on indium tin oxide (ITO)-coated glass (CB-40IN-S111, Delta Technologies). A dielectric layer of SU-8 (GM 1040, Gersteltech) was patterned on top of the electrodes, followed by a hydrophobic coating (Fluoropel PFC1101V, Cytonix) applied using a stencil during spin coating. The microchannel walls were constructed using double-sided adhesive tape (8146-1, 3M) cut to shape using a cutter printer (Cameo 4, Silhouette), following a rapid prototyping method previously reported.[35] The channel structure was sandwiched between two ITO-coated glass slides, with the top slide drilled to create inlet and outlet ports (~1 mm in diameter). To control the position of the preconcentrated plug, two cationic permselective membranes (Nafion 1100 W, Sigma-Aldrich), each 200 μm wide, were patterned inside the main microchannel upstream and downstream of the intersection with the side channel, at a spacing of 5 mm. The use of two membranes facilitated control over the location of the preconcentrated plug,[9,10,36,37] although fine-tuning still required manual adjustment. The main channel included a curved segment designed to prevent contact between the EWOD electrode feed lines and the membranes. The platform fabrication process is presented schematically in Fig. S1. The DMF electrodes were actuated using a function generator (Siglent Technologies SDG 2042X) and a voltage amplifier (Trek 2220), with manual control *via* a custom-built switching system. The Nafion ion-selective membranes were biased using a voltage source (Keithley 2636a) and 30AWG wires were soldered to the electrode pads for connectivity.

ICP enrichment and depletion diffusion layers were visualized by adding negatively charged, 1 μM pH-independent (as previously reported[9]) Dylight molecules (Dylight 488, Thermo Scientific) to a 10 μM KCl solution with a conductivity of 2 μS cm^{-1}. Demonstrations of manipulating bioparticles inside the platform were done using 1 ng μl^{-1} fluorescently tagged 23-mer DNA (5′-6-FAM-TAA AGG TGC TCA TCA TGG GAA AG-3′; IDT, Coralville, IA, USA) and 100 μg ml^{-1} recombinant *Aequorea victoria* GFP protein (ab84191, Abcam, Cambridge, UK) as the target analytes. Both analytes were added to a 10 μM KCl solution with a conductivity of 2 μS cm^{-1}. Calibrations curves relating measured fluorescence intensity to molecular concentration were established for DyLight fluorescent molecules, DNA, and GFP, as shown in Fig. S2. Imaging was conducted using a spinning disc confocal microscopy system (Yokogawa CSU-X1) integrated with an inverted microscope (Eclipse Ti-U, Nikon) and a camera (Andor iXon3). Flow within the main microchannel was driven by a hydraulic pressure gradient between the inlet and outlet ports, with an approximate height difference of 2 mm. Flow velocity was characterized using particle image velocimetry (PIV) with ImageJ and MATLAB software.

Numerical simulations

The numerical simulations were based on the approach described in ref. 6. A fully coupled, two-dimensional (2D), time-dependent model was implemented using the finite-element software COMSOL (V6.3). The governing equations for the simulation include the continuity of ions expressed by the Nernst–Planck relation:

$$\frac{\partial c_i}{\partial t} = -\nabla\cdot j_i,\; j_i = -\left(D_i\nabla c_i + Z_i\frac{F}{RT}D_i c_i\nabla\phi\right) + \boldsymbol{u}c_i,\; i = 1,2,3 \quad (1)$$

along with the Poisson equation for the electric potential:

$$-\nabla\cdot(\varepsilon\nabla\phi) = \rho_{\mathrm{e}},\; \rho_{\mathrm{e}} = F\sum_i z_i c_i \quad (2)$$

and the Stokes and continuity equations:

$$\rho\frac{\partial \boldsymbol{u}}{\partial t} = -\nabla p + \eta\nabla\cdot\nabla\boldsymbol{u} - \rho_e\nabla\phi,\; \nabla\cdot\boldsymbol{u} = 0. \quad (3)$$

Here, c_i is the concentration of species i, F is the Faraday constant, R is the universal gas constant, T is absolute temperature, $\boldsymbol{u}$ is fluid velocity vector, p is pressure, ε is solution permittivity, ρ is solution mass density, and η is its dynamic viscosity. Species indices were assigned as follows: $i = 1$ for K$^+$, $i = 2$ for Cl$^-$, and $i = 3$ for the negatively charged Dylight molecules. Diffusion coefficients and valences were set as $D_1 = D_2 = 2 \times 10^{-9}$ m^2 s^{-1},[38] $D_3 = 3 \times 10^{-10}$ m^2 s^{-1},[39] $z_1 = -z_2 = -z_3 = 1$.

The simulation geometry represented a geometrically scaled-down, two-dimensional representation of the intersection between the main and side microchannels. Two 100 μm-wide cation-selective membranes were placed inside the main microchannel (length = 1.7 mm, width = 125 μm) with an intermembrane spacing of 1 mm, upstream and downstream of the side microchannel (width = 75 μm, length = 500 μm). In Fig. 2, the side channel terminated with a wall boundary condition ($\boldsymbol{u} = 0$, $\nabla c_i\cdot\boldsymbol{n} = 0$, where $\boldsymbol{n}$ is the unit normal vector to the surface), while in Fig. 3, the end was changed to a velocity outlet (1.6 mm s^{-1}) to simulate the convective flux immediately following an EWOD-induced droplet extraction. For the simulation shown in Fig. 4, the side channel length was 150 μm, and a temporary internal wall boundary was placed midway along its length. This internal wall was removed at normalized time $\mathrm{Fo_m} = 0.533$, and the side channel's end was changed to a velocity outlet (1.6 mm s^{-1}). Simulation geometries are provided in Fig. S3. Initial ion concentrations were defined as $c_{1,0} = c_{2,0} = 0.001$ mol m^{-3} and $c_{3,0} = 5 \times 10^{-6}$ mol m^{-3}. At the membrane interface, boundary conditions assumed ideal cation permselectivity: no anion penetration, a fixed cation concentration ($c_1 = N\cdot c_{1,0}$), and a Donnan potential ($-RT/F\cdot\ln(N)$) with $N = 10$. The main microchannel inlet was set to constant bulk concentrations $c_i = c_{i,0}$ for all species ($i = 1, 2, 3$) and a uniform inlet velocity of 5 μm s^{-1}. Open boundary conditions ($\nabla c_i\cdot n = 0$, $\mathrm{d}u/\mathrm{d}x = 0$) were applied at the

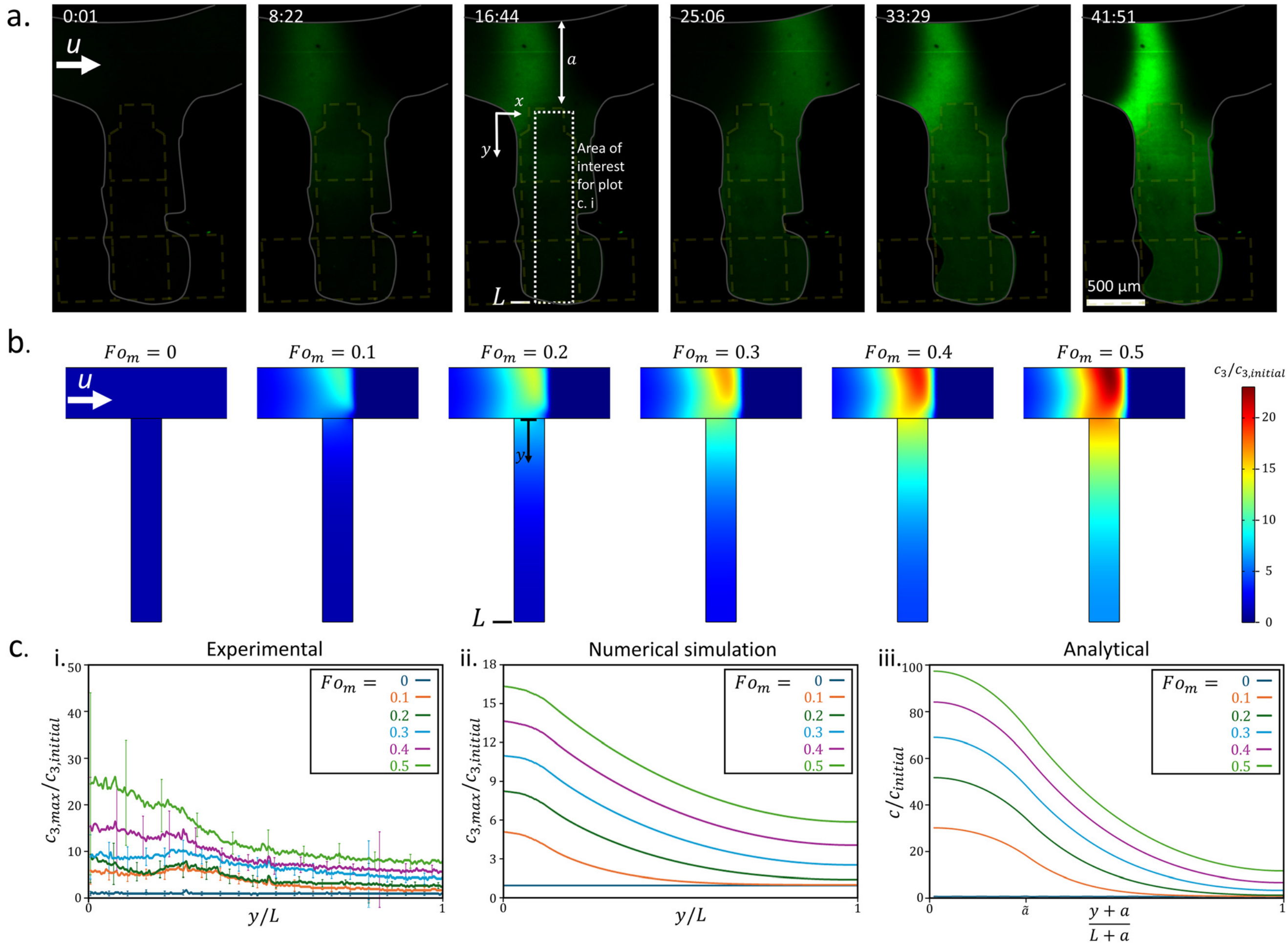

Fig. 2 The diffusion of the preconcentrated plug into the largely stagnant side channel. (a) Experimental visualization of the creation of a preconcentrated fluorescent molecule plug generated *via* ion concentration polarization within the horizontal microfluidic channel and its simultaneous diffusion into the largely stagnant side channel. (b) Numerical simulation of plug formation and diffusion for normalized (by the diffusion length) time intervals corresponding to those in the experiment in part a. (c) Normalized concentration profiles of fluorescent molecules (relative to their initial concentration), represented as the maximum concentration along the *x*-axis, plotted against the normalized side channel length for different $\mathrm{Fo_m}$ from: i. experiment, ii. numerical simulation, iii. analytical solutions. The error bars in Fig. 2c, i represent the cross-sectional variability of the fluorescence intensity at each *y*-coordinate.

outlet. All other channel walls were treated with no-penetration, no-slip, and electrical insulation conditions.

Analytical model

The analytical solution for the diffusion of the electrokinetically preconcentrated molecules into the side microchannel was developed to qualitatively align with the experimental observations and numerical simulations. Observations from experiments and numerical simulations indicated an approximately stagnant solution within the side microchannel after its first quarter (Fig. S4). Hence, for simplification the side microchannel was assumed stagnant, having a uniform molecular concentration across its cross-section. As a result, a one-dimensional (1D) time-dependent diffusion model, excluding convective terms, was used along the channel length.

Furthermore, the rate of formation of the preconcentrated fluorescent molecule plug was represented as a volumetric source of molecules denoted as $\dot{N}(y)$, where y denotes the position along the side microchannel, including the width of the main channel, measured from the far wall of the main channel to the end of the side channel (Fig. 2a); the side channel length is L = 1.6 mm. The source was located within the main channel, while its width (a) equals that of the side channel (w), as presented in Fig. S5. Thus, the governing diffusion equation was as follows:

$$\frac{\partial c}{\partial t} = D\frac{\partial^2 c}{\partial y^2} + \dot{N}(y),\ t > 0,\ -a < y < L \tag{4}$$

$$\dot{N}(y)=\begin{cases} g & ,-a<y<0 \\ 0 & ,0\le y<L \end{cases}$$

where $c(y,\ t)$ is the molecules concentration, $D = 3 \times 10^{-10}$ m^2 s^{-1},[39] is their diffusion coefficient, $a = 600$ μm is the main channel's width, $g=\frac{c_0 u}{w}$ is the constant uniform volumetric source of molecule generation, where $u = 42$ μm s^{-1} is the liquid velocity inside the main channel, and $w = 600$ μm is the side channel's width. The initial condition assumed uniform concentration 1×10^{-3} mol m^{-3}. Thus, the volumetric source term describing molecular accumulation represents the (ideally assumed, for simplicity) trapping of molecular species within the preconcentrated plug, accounting for their time-dependent accumulation at the specified location. In addition, a boundary condition of zero flux of molecules was used at both ends of the side channel $\frac{\partial c}{\partial y}\Big|_{y=-a}=\frac{\partial c}{\partial y}\Big|_{y=L}=0$.

Results and discussion

Droplet extraction from a hybrid continuous-discrete microfluidic platform

As shown in Fig. 1, the side channel serves as an interface between the main microchannel and the EWOD electrode array. The hydrophobic layer in the EWOD section acts as a capillary barrier, partially covering electrode #2 (Fig. 1b). Upon activation of electrode #2, the liquid front is drawn onto the electrode. Subsequent activation of downstream electrodes (*e.g.* electrode #5) moves the liquid further along the EWOD array. This process eventually forms necking in the liquid and generates discrete droplets of volumes as small as 6 nL and larger (see Fig. S6). Experimental results (Fig. S6) showed that successful droplet generation requires the liquid front to be deflected sideways from its original path, establishing a three-phase contact line on both sides of the liquid. If the liquid is pulled strictly along the original path, the microchannel effectively acts as an infinite reservoir, generating back pressure that suppresses neck formation—a critical step for droplet generation—thus preventing droplet formation.

Preconcentrated plug formation and its diffusion to the side channel

For the generation of molecularly preconcentrated droplets, we used a solution of 1 μM negatively charged green Dylight fluorescent molecules (Dylight 488, Thermo Scientific) as the target analyte in 10 μM KCl, with a conductivity of 2 μS cm^{-1}. The flow in the main microchannel was driven by a hydraulic pressure difference and analyzed using particle tracking with ImageJ software to track tracer fluorescent particles added to the solution, yielding an average flow velocity of ∼42 ± 6 μm s^{-1} just before applying voltage to the ion-selective membranes (Fig. S7). Velocity measurements included only the horizontal flow component, calculated as the average velocity of 6 particles tracked at different locations across the main channel cross-section, upstream of the side channel. Examination of the experimentally generated flow streamlines – captured using a long camera exposure time – shows that the main channel flow penetrates ∼400 μm into the 1.6 mm long side channel (Fig. S4a). This observation was supported by numerical simulations, which exhibited similar qualitative behavior (Fig. S4b), confirming that the side channel remained stagnant beyond the initial 400 μm. Therefore, to examine the diffusion of the preconcentrated plug under stagnant conditions in the side channel, the channel was extended to provide sufficient length for the plug to diffuse away from the main channel intersection, where convective effects dominate. To achieve this, the first three EWOD electrodes (electrodes #1, 2, 5 – each ∼0.5 mm in size) were activated to draw the side channel's end onto them, elongating the side channel to 1.6 mm. Afterward, the three electrodes were turned off, and the back pressure from the main channel maintained the liquid's front thereon, as seen in Fig. 2a.

Subsequently, a 60 V DC voltage was applied between the ion-selective membranes, with the anodic side upstream and the cathodic side downstream of the side channel. This resulted in the formation of a preconcentrated plug of fluorescent molecules. The position of the plug was controlled either by varying the voltage in 10 V increments or by modifying the pressure difference driving the channel flow through addition or removal of solution from the inlet and outlet reservoirs. The effects of flow velocity and applied voltage on the plug's location – through their influence on the depletion layer length generated from the cathodic side when the plug is located near its upstream edge – were previously studied.[40,41] These studies showed that increasing the applied voltage enhances electrokinetic repulsion of fluorescent molecules from the downstream cathodic membrane, whereas higher flow rates promote their downstream transport toward the membrane.

As shown in Fig. 2a, the concentrated plug accumulated at the intersection between the main and side channels, with its fluorescent intensity increasing over time. Simultaneously, the accumulating plug diffused into the largely stagnant side channel, increasing the fluorescent intensity throughout the side channel over time. Additionally, the manual adjustments of the plug position during its accumulation are visible. Fig. 2c, i depicts the normalized maximum concentration along the side channel's width (x-axis), relative to the initial concentration, as a function of the normalized side channel length (y/L), where L is the total length of the side channel (1.6 mm). The maximum concentration along the side channel's width was used to avoid the effects of plug position adjustments on the concentration measurements along the side channel. A rectangular region of interest was defined to facilitate fluorescent intensity measurements within the side channel, as shown in Fig. 2a, 16:44 (minutes:seconds). The corresponding time intervals, shown in Fig. 2a, are

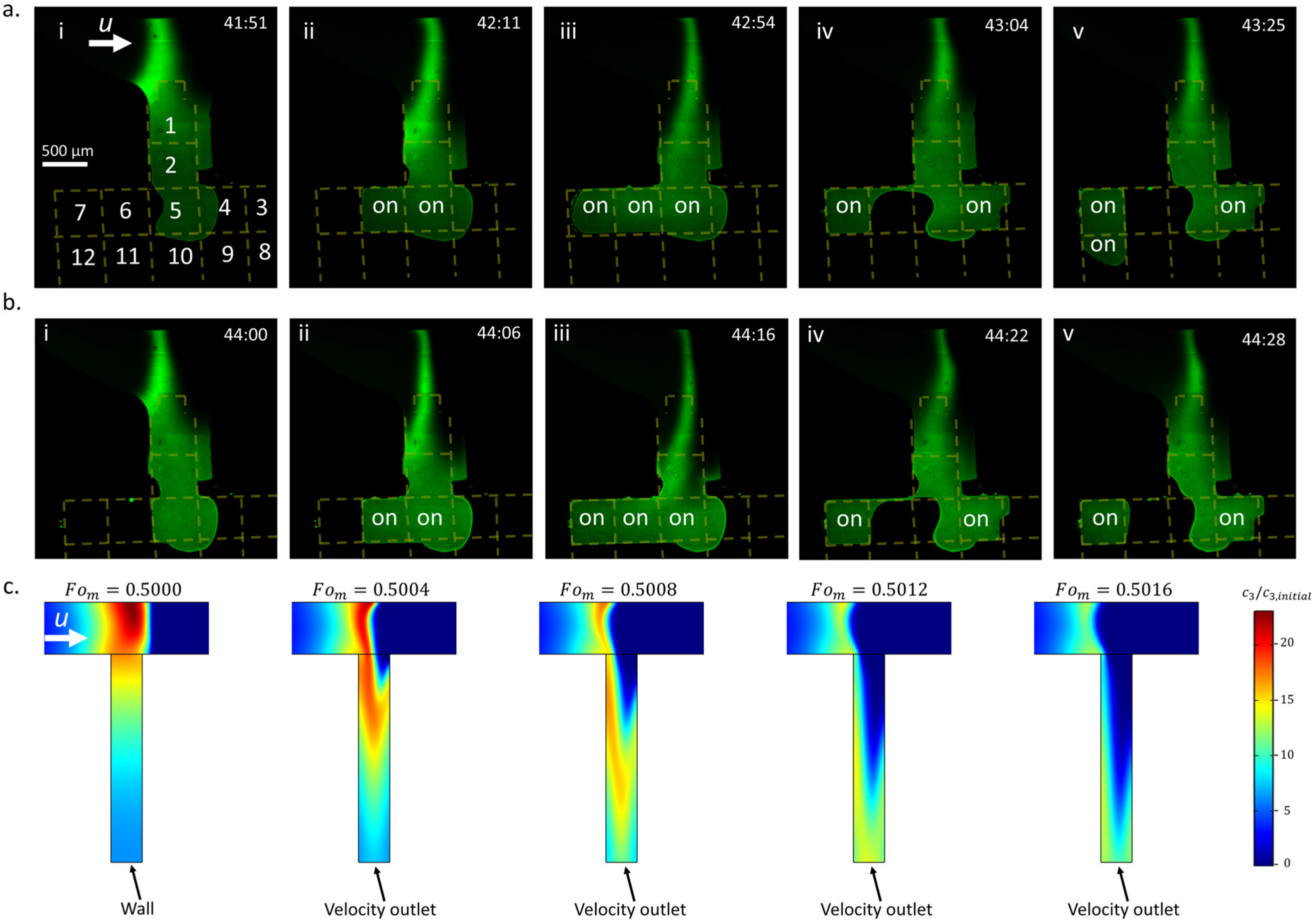

Fig. 3 Extraction of the preconcentrated plug of fluorescent molecules. Time sequence of the generation process of concentrated droplets *via* electrowetting-on-dielectric. (a) Droplet generation (steps (i)–(v)) starting after the diffusion of the preconcentrated plug to the side channel presented in Fig. 2a (41 min and 51 s after ICP initiation). (b) Generation (steps (i)–(v)) of a second droplet starting shortly after generating the first droplet in Fig. 3a, i–v. (c) Numerical simulation of the convective pull of the plug to the side channel starting from the last normalized time interval (Fo_m = 0.5) presented in Fig. 2b. At this instant, the wall boundary condition (*i.e.* $u = 0$, $\partial c/\partial x = 0$), at the end of the side channel changed into a velocity outlet.

normalized as the Fourier number for mass transport $Fo_m = Dt/L_s^2$ where D ($=3 \times 10^{-10}$ m^2 s^{-1} [39]) is the diffusion coefficient of the fluorescent molecules in water, t is the time, and L_s (=1.2 mm) is the length of the stagnant part of the side channel, after the first 400 µm where convective effects dominate, as mentioned above. As seen in Fig. 2c, i, the plug concentration (at the side channel entrance) increased over time, reaching a factor of ~25 at Fo_m = 0.5 (~42 minutes). Simultaneously, the concentration of fluorescent molecules at the end of the side channel increased by a factor of ~8. A video of the experimental process of forming the plug and its simultaneous diffusion is available in video S1.

Numerical simulations were also conducted to understand the formation of the ICP preconcentrated plug at the intersection and its diffusion into the side channel. In the simulation, a voltage of 98 V DC was applied to the ion-selective membranes, with a velocity inlet boundary condition of 0.7 µm s^{-1} in the main channel. These parameters were found to form a sufficient plug for observing its diffusion to the side channel, while maintaining its location at the intersection. The specific numerical values were therefore chosen to reproduce qualitatively similar plug-location behavior, rather than to match the experimental voltages quantitatively. As mentioned previously, the smaller-scale channel configuration was used in the simulation to reduce the computational load. Fig. 2b presents the results of the numerical simulation for normalized time intervals of the smaller scale numerical simulation system corresponding to those presented in Fig. 2c, i of the larger scale experimental system, considering the different channel length (L) and time (t) values accordingly. Specifically, the length used for the normalized time intervals in the numerical simulation is the entire side channel's length (L = 500 µm) of the simulation model (Fig. S3a), since the flow velocity in the main channel was sufficiently low to result with stagnant conditions along the entire side channel. Similarly to the experimental Fig. 2c, i, and ii shows the normalized maximum concentration along the side channel's width, relative to the initial concentration, as a function of the normalized side

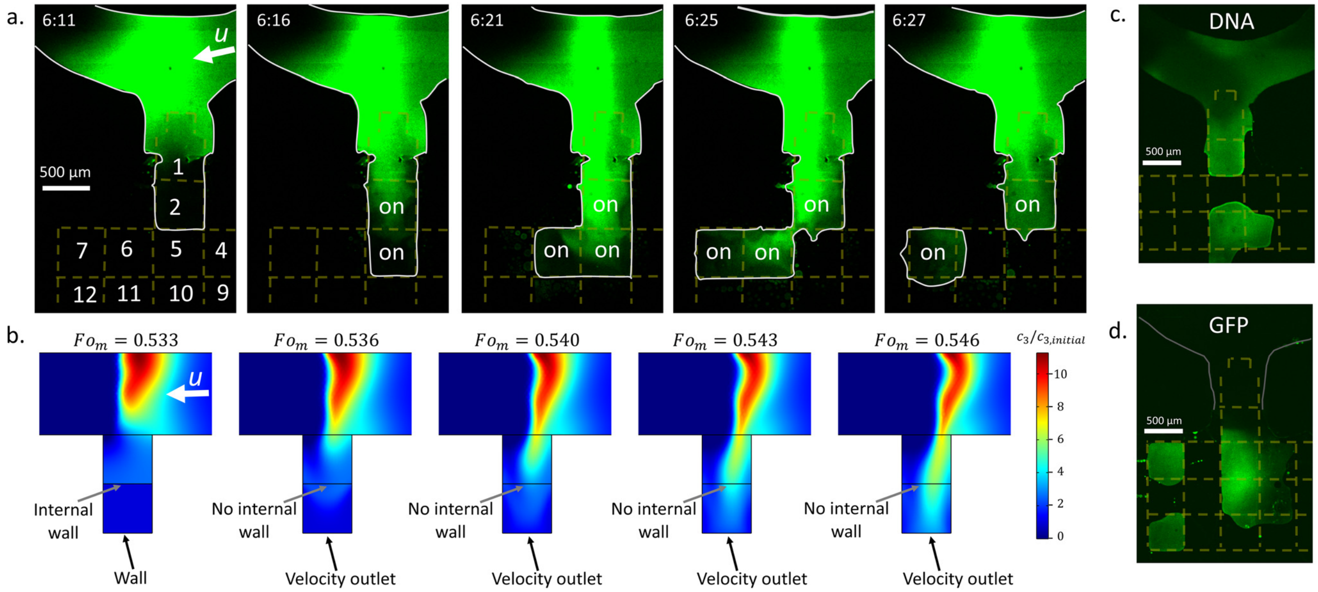

Fig. 4 Generation of a droplet using electrowetting-on-dielectric with only convective transport of an ICP-preconcentrated plug without diffusion into a side channel. (a) Experimental visualization of droplet generation, where the ICP-preconcentrated plug of fluorescent molecules is transported to the side channel solely by convective pulling, without allowing diffusion into the side channel. (b) Numerical simulation of convective transport of the ICP-preconcentrated plug into the side channel, where convection dominates over diffusion during this time interval (Pe > 1). (c) DNA-extracted preconcentrated droplet: experimental visualization of a DNA-enriched droplet exhibiting increased concentration *via* the convective pulling protocol. (d) GFP-extracted preconcentrated droplet: experimental visualization of GFP-enriched droplets, in which concentration enhancement was achieved under similar convective transport conditions.

channel length (y/L). As shown in this figure, the plug accumulated over time while diffusing into the side channel. The concentration at the entrance of the side channel ($y/L = 0$) increased by a factor of approximately 16 at $\mathrm{Fo_m} = 0.5$, while at the same time, the concentration at the end of the side channel ($y/L = 1$) increased by a factor of approximately 6. While in qualitative agreement, the quantitative differences between the obtained normalized concentrations of the simulation and experiment can be attributed to the differences in the channel dimensions (*e.g.* a channel width of 75 µm in the simulation *versus* 600 µm in the experiment), and operating parameters (applied voltage and flow velocity) as well as the fact that the numerical simulations are 2D while the experiments are 3D. This may also be attributed to the fluctuating concentrations and reduced concentration gradients observed in the experimental accumulation region of the main microfluidic channel, compared with the numerical simulations (see Video S2).

Following the formulation presented above for the analytical model, the following solution (more details in the SI) was obtained for the 1D normalized (relative to the initial concentration c_0) concentration $C = c/c_0$:

$$C(\eta,\tau) = 1 + A_0 + \sum_{n=1}^{\infty} A_n e^{-(n\pi)^2\tau}\cos(n\pi\eta) + \begin{cases} \tilde{g}\left[\tilde{a}\tau + \frac{1}{2}(\tilde{a}-1)\eta^2\right] & ,0<\eta<\tilde{a} \\ \tilde{g}\left[\tilde{a}\tau + \frac{1}{2}\tilde{a}(\eta-1)^2 + \frac{\tilde{a}}{2}(\tilde{a}-1)\right] & ,\tilde{a}<\eta<1 \end{cases} \tag{5}$$

$$A_0 = \tilde{g}\frac{1}{6}\tilde{a}(1-\tilde{a})(2-\tilde{a}) \tag{6}$$

$$A_n = -\frac{2\tilde{g}\left[2\sin(n\pi\tilde{a}) + \tilde{a}\sin(n\pi)\left(-2 + n^2\pi^2(\tilde{a}-1)\right)\right]}{n^2\pi^2\left(\cos(n\pi)\sin(n\pi) + n\pi\right)} \tag{7}$$

where $\eta = \frac{y+a}{L+a}$, $\tau = \frac{Dt}{(L+a)^2}$, representing the normalized spatial and temporal variables, respectively, $\tilde{g} = \frac{gL^2}{c_0 D}$ is the normalized uniform source of molecules, and $\tilde{a} = \frac{a}{L+a}$ denotes the normalized extent of the uniform molecular source. The resulting analytical concentration profiles, calculated for normalized time intervals matching those used in the experimental and numerical analyses, are shown in Fig. 2c, iii. For consistency with the time normalization in the experimental and numerical plots the analytical normalized time depicted in Fig. 2c is taken as $\mathrm{Fo_m} = \frac{Dt}{L^2} = \tau\frac{(L+a)^2}{L^2}$. As illustrated, the presence of a uniform internal source of fluorescent molecules confined to the region between $\eta = 0$ and $\eta = \tilde{a}$ leads to a progressive increase in concentration over time, qualitatively capturing the accumulation behavior of the ICP plug within the main channel. Simultaneously, diffusion of molecules from this source region into the adjacent domain ($\eta > \tilde{a}$) results in a gradual rise in concentration within the stagnant side channel, replicating the diffusive transport observed in both the experiments and numerical simulations. The implementation of zero-flux boundary conditions at both the beginning and the end of the 1D domain ($\eta = 0$ and $\eta = 1$ respectively) is evidenced by the vanishing concentration gradients. A convergence analysis confirmed that the first ten terms of the series expansion are sufficient to accurately capture the solution (see SI). A qualitative agreement was obtained when compared to numerical simulation results, however, the analytical solution exhibits higher concentration values. This discrepancy may be attributed to the idealized assumption of complete ICP-induced trapping of molecules within the plug in the 1D analytical model (eqn (4)), whereas in the 2D numerical model, molecular escape from the ICP-induced trap is possible.

As illustrated in Fig. 2, qualitative agreement is observed among the experimental, numerical, and analytical results for the normalized concentrations along the side channel length (Fig. 2c). Discrepancies near the side channel entrance ($y/L = 0$) arise from the inherent challenge of precisely positioning the preconcentrated plug at the entry point. Although the plug's location was regulated by manually adjusting either the flow velocity or the voltage applied to the ion-selective membranes, slight variations around the intersection remained. Nevertheless, there is an overall agreement in the way the normalized concentration along the channel and its increase over time behaves in both experiments and numerical/theoretical analysis. Furthermore, at the end of the side channel ($y/L = 1$), a boundary condition of zero flux is observed for all methods, as the slope of the concentration *versus* channel length is zero at this point for all times in agreement to what is expected from the fact that the liquid front at the end of the side channel, which was held by a hydrophobic barrier, is interfacing air.

Molecularly concentrated droplet generation and convection-driven plug extraction

At this stage, the EWOD electrodes were activated (440 V_{pp} at 20 kHz), while the DC voltage on the ion-selective membranes was maintained. Initially, electrode #5 – located within the 3 × 5 array and interfacing with the side channel – was activated along with its adjacent electrode to the left (electrode #6), to draw the liquid front toward the side channel (Fig. 3a, ii). Subsequently, electrode #7 was activated to further advance the liquid front (Fig. 3a, iii). To initiate droplet formation, electrode #4 (adjacent to the right of the side channel's end) was activated, while electrodes #5 and #6 were deactivated, creating the necking necessary for droplet cutting[13] (Fig. 3a, iv). Finally, electrode #12 – positioned below the farthest left operating electrode – was activated to move the left liquid front forward and generate a 10 nL concentrated droplet (Fig. 3a, v), which was then transported across the EWOD electrode array. The average fluorescent molecule concentration inside the droplet was approximately ∼11 times higher than the initial concentration in the solution. During liquid extraction from the side channel, a strong convective pull was observed on the preconcentrated plug within the main channel. Hence, the fluorescent molecules concentration inside the droplet was higher than that at the end of the side channel just before starting the process of pulling the liquid onto the EWOD platform to generate the droplet (8-fold, Fig. 2a, 41:51 (minutes:seconds)). The Peclet number calculated for the convective pull (Fig. 3a, 41:51 (min:s)) is $\mathrm{Pe}_\mathrm{m} = \frac{uD_\mathrm{h}}{D} = 39.6$, indicating the dominance of convective transport over diffusion of the fluorescent molecules. Here, $u \sim 0.25\ \mathrm{mm\ s^{-1}}$ is the approximate velocity of the liquid front during EWOD pulling. This velocity was estimated from the time required (∼1 s; two frames at a frame rate of 500 ms per frame) for the liquid front to transverse one electrode (500 μm, from electrode #5 to #6). The diffusion coefficient of the fluorescent molecules is $D = 3 \times 10^{-10}\ \mathrm{m^2\ s^{-1}}$.[39] The hydraulic diameter over electrode #6 is $D_\mathrm{h} = \frac{4(hw)}{(2h + 2w)} = 47.62\ \mu\mathrm{m}$, where $h = 25\ \mu\mathrm{m}$ is the channel gap and $w = 500\ \mu\mathrm{m}$ is the electrode width.

Following the generation of the first concentrated droplet, a second droplet was extracted after a shorter accumulation time, before the regenerated preconcentrated plug in the main channel had fully developed or sufficiently diffused into the side channel (35 seconds after Fig. 3a, v). This is evident from the narrower plug observed prior to the second droplet (Fig. 3b, i) compared to the wider plug before the first droplet (Fig. 3a, i). Despite the shorter accumulation time, the second droplet (∼6.4 nL) reached an average concentration of ∼11 times higher than the initial solution concentration. As shown in Fig. 3b, the convective pull during droplet formation preserved the plug's concentrated state, eliminating the need for additional diffusion time. The complete sequence of reproducing three consecutive droplets is shown in video S3.

This convective pull of the plug was also investigated through numerical simulations (Video S4). At normalized time $\mathrm{Fo}_\mathrm{m} = 0.5$ (Fig. 2b), side channel's boundary condition was switched from a wall to a 1.6 mm $\mathrm{s^{-1}}$ velocity outlet, simulating EWOD-induced flow. As shown in Fig. 3c, this sharply reduced the time required to increase concentration at the channel end, doubling it between $\mathrm{Fo}_\mathrm{m} = 0.5$ and $\mathrm{Fo}_\mathrm{m} = 0.5012$, compared to diffusion alone.

The plug also narrowed more quickly than it accumulated, consistent with both experimental and simulation results. Although the second droplet (Fig. 3b) was expected to be more concentrated than the first (Fig. 3a), it also pulled in downstream dilution, resulting in similar final concentrations. These findings demonstrate that introducing a preconcentrated plug into a stagnant side channel, followed by droplet generation, effectively extracts enriched volumes. While convective pull causes some dilution, concentrations remain relatively high (∼11 areal averaged factor) compared to the initial concentration of the solution. Importantly, for subsequent droplets, convective pull alone maintains enrichment, eliminating the need for additional diffusion or accumulation.

Plug formation and concentrated droplet generation without diffusion of the plug into a side channel

To further investigate droplet generation from an ICP-preconcentrated plug, a shortened side channel was used on a second platform, that could not sustain stagnant conditions or support diffusion, as seen in the longer channel (Fig. 2). As a result, plug extraction relied solely on convective pulling during droplet generation. A DC voltage of 70 V DC was applied across the ion-selective membranes (anode upstream, cathode downstream), similar to Fig. 2 and 3. Unlike the previous setup, the side channel covered only the first EWOD electrode (electrode 1, Fig. 4a), rather than extending across three. After plug accumulation and manual positioning near the intersection, electrode #2 was activated (500 V_{pp} at 20 kHz) to pull the plug closer to the intersection. This ensured that the convective pull during droplet generation would draw in the concentrated plug, rather than mostly diluted solution from downstream. Once the side channel covered electrode #2, that electrode was turned off, and the liquid front remained pinned due to back pressure from the main channel. At this point (Fig. 4a, 6:11 (min:s)), while maintaining the voltage across the ion-selective membranes, the EWOD electrodes were actuated to initiate droplet generation, similarly to the previous experiment presented in Fig. 3. The Peclet number calculated for the convective pull (Fig. 4a, 6:11 (min:s)) is $\mathrm{Pe_m} = \frac{uD_\mathrm{h}}{D} = 158$, indicating the dominance of convective transport over diffusion of the fluorescent molecules. Here, $u \sim 1$ mm s^{-1} is the approximate velocity of the liquid front during EWOD pulling. This velocity was estimated from the time required (~500 ms; within a single frame at a frame rate of 500 ms per frame) for the liquid front to transverse one electrode (500 μm, from electrode #2 to #5).

In contrast to the previous experiment shown in Fig. 3a, the liquid did not remain on electrode #2, interfacing the side channel and the electrode array, when it was turned off. This behavior likely resulted from lower back pressure in the main and side channels, which may have been insufficient to hold the liquid front in place. Consequently, it was unnecessary to pull the liquid to the right to cut a droplet, as was done previously. Instead, simply activating the leftmost electrode (electrode #7) and the electrode in the side channel (electrode #2) was sufficient to generate a droplet (Fig. 4a, 6:27 (min:s)). The resulting droplet had a volume of 7.5 nL and exhibited an average fluorescent concentration approximately twice that in the side channel just before plug pulling (Fig. 4a, 6:11 (min:s)). As shown in Fig. 4a, the plug narrowed during convective pulling because the pull rate exceeded the plug's accumulation rate. Simultaneously, the convective force also drew in diluted solution from downstream of the plug into the side channel, limiting further increases in droplet concentration. These trends are consistent with those observed in Fig. 3. A higher voltage was required for EWOD actuation compared to the previous experiment (Fig. 3a and b), which led to the formation of small satellite droplets near the liquid front, as seen in Fig. 4a.[42,43] This increased voltage requirement may be attributed to surface impurities, such as slight variations in the dielectric or hydrophobic coating thickness, which introduced localized resistance that the EWOD force had to overcome. The droplet generation process is also demonstrated in Video S5. Numerical simulations were also conducted to examine the generation and convective pulling of the ICP preconcentrated plug into the side channel, using normalized time increments ($\Delta\mathrm{Fo_m} = 0.0034$) small enough to minimize diffusion effects (see Video S6). These increments matched those used in the experimental images of Fig. 4a, adjusted for the differing side channel lengths: 600 μm in the experiment (Fig. 4a) and 75 μm in the simulation (Fig. 4b). A 98 V DC voltage was applied across the ion-selective membranes, and a 0.7 μm s^{-1} velocity inlet boundary condition was set in the main channel, consistent with prior simulations (Fig. 2 and 3). During plug formation, an internal wall midway along the side channel restricted diffusion, mimicking the diluted region observed experimentally at time t = 6:11 (min:s) (Fig. 4a). After sufficient plug accumulation (Fig. 4b, $\mathrm{Fo_m} = 0.533$), this wall was removed, and the channel outlet was set to a velocity boundary of 1.6 mm s^{-1}.

The simulation results (Fig. 4b) qualitatively align with the experiment, showing that convective pulling significantly increased concentration at the side channel end—by a factor of two—while narrowing the plug. However, it also drew in diluted downstream solution, limiting the maximum concentration. These findings show that convective pulling enables rapid generation of concentrated droplets without relying on diffusion, though the concurrent intake of diluted solution constrains the overall concentration enhancement.

Utilizing the convective pulling method, experiments were conducted on two additional platforms to demonstrate the localized enrichment and discrete droplet generation of fluorescently tagged 23-mer DNA and green fluorescent protein (GFP). To initiate ICP-based DNA preconcentration within the main microfluidic channel, a potential difference of 45 V was applied across the ion-selective membranes. Subsequently, the EWOD array was sequentially actuated to transport the preconcentrated plug onto electrodes #10 and #11. By maintaining these electrodes in an active state, the liquid's front was pinned over them while a mechanical plunger induced hydrodynamic backflow toward the channel inlet. This coordinated action resulted in the formation of a 29 nL droplet (Fig. 4c) exhibiting an areal-averaged 8-fold increase in DNA concentration relative to the initial solution concentration (see Video S7). For this experiment, the device featured a channel gap of 50 μm to demonstrate the protocol's adaptability to larger microfluidic gaps.

A similar protocol was applied for the manipulation of GFP molecules. A potential difference of 80 V was applied across the ion-selective membranes to generate a preconcentrated plug of GFP. Upon actuation of the EWOD electrodes, the plug was translated onto the digital microfluidic array. Activation of electrodes #7, #11, and #12 then enabled lateral fluid pulling, resulting in the formation of a 12 nL droplet with an areal-average 2.5-fold enhancement in GFP concentration relative to the initial solution concentration. The droplet was subsequently split into two smaller droplets, as shown in Fig. 4d (see Video S8). The results were validated across four independent devices, demonstrating reproducible on-chip molecular enrichment and discrete extraction of concentrated droplets. Droplet concentration depends on coupled parameters—including plug morphology, flow rate, and channel geometry—whose optimization is beyond the scope of this study. As a proof of concept, this work focuses on extracting and preserving enriched analytes from continuous flow and assessing droplet enrichment relative to the initial bulk concentration. This strategy overcomes a key limitation of ICP-based preconcentration, where enriched plugs rapidly disperse once the voltage is removed. Isolating the plug as a discrete droplet enables downstream analysis without continuous flow or sustained electrical bias.

Conclusions

We have introduced a novel hybrid platform that integrates continuous and digital microfluidics to generate preconcentrated discrete droplets from ICP-based preconcentration occurring within a continuous medium. Initially, we described an assay in which a preconcentrated molecular plug is formed within a microchannel *via* ICP, then diffuses into a dead-end side channel, from which a preconcentrated droplet is subsequently generated using EWOD. The formation and diffusion of the preconcentrated plug were further investigated using both numerical simulations and an analytical solution, both of which showed qualitative agreement with the experimental results. We also investigated the effect of convective pulling on plug transport into the side channel through both experimental and numerical studies, aiming to replace the slow diffusion process with a much faster convective mechanism. Our results show that convective pulling alone can generate droplets with increased concentrations. However, higher concentrations were achieved when the plug was allowed to diffuse into the side channel prior to convective extraction. While precise positioning of the preconcentrated plug relative to the side channel was achieved manually in this study, future effort could employ closed-loop feedback control or pre-calibrated automation to improve reproducibility and facilitate further development of this approach as a bioanalytical tool.

These findings demonstrate that the proposed hybrid platform offers a reliable and efficient approach for extracting discrete volumes of preconcentrated solutions. It enables the direct generation of preconcentrated droplets from microchannels into an air environment, without the need for an oil medium. This capability is expected to substantially improve the integration of continuous microfluidic capabilities, such as bioparticle preconcentration, with the ability to extract these preconcentrated plugs from the system *via* the EWOD platform.

Conflicts of interest

There are no conflicts to declare.

Data availability

The data supporting this article have been included as part of the supplementary information (SI).

Supplementary information is available and includes the fabrication process (Fig. S1), calibration of measured fluorescence intensity (Fig. S2), geometry of the numerical simulations (Fig. S3), experimental and numerical flow streamlines (Fig. S4), geometry of the analytical solution (Fig. S5), time sequences showing the generation of a droplet from the stagnant side channel (Fig. S6), flow velocity measurement using particle tracking (Fig. S7), analytical model formulation and derivation, convergence of the analytical solution (Fig. S8), and Videos S1–S8. See DOI: https://doi.org/10.1039/d5lc00647c.

Acknowledgements

We thank Tel-Aviv University nano-center for assisting with the fabrication of the chips. We acknowledge the financial support of the Ministry of Innovation, Science & Technology (MOST), Israel [grant #4768]. We thank Prof. Touvia Miloh (Tel Aviv University) for his assistance in developing the analytical solution.

References

1 I. Rubinstein and L. Shtilman, *J. Chem. Soc., Faraday Trans. 2*, 1979, **75**, 231.
2 G. Yossifon, P. Mushenheim, Y.-C. Chang and H.-C. Chang, *Phys. Rev. E: Stat., Nonlinear, Soft Matter Phys.*, 2009, **79**, 046305.
3 Q. Pu, J. Yun, H. Temkin and S. Liu, *Nano Lett.*, 2004, **4**, 1099–1103.
4 T. A. Zangle, A. Mani and J. G. Santiago, *Langmuir*, 2009, **25**, 3909–3916.
5 S. Park and G. Yossifon, *Anal. Chem.*, 2020, **92**, 2476–2482.
6 S. Park, D. Kaufman, H. Ben-Yoav and G. Yossifon, *Anal. Chem.*, 2024, **96**, 6501–6510.
7 M. M. Gong, R. Nosrati, M. C. San Gabriel, A. Zini and D. Sinton, *J. Am. Chem. Soc.*, 2015, **137**, 13913–13919.
8 S. A. Hong, Y. J. Kim, S. J. Kim and S. Yang, *Biosens. Bioelectron.*, 2018, **107**, 103–110.
9 S. Park, B. Sabbagh, R. Abu-Rjal and G. Yossifon, *Lab Chip*, 2022, **22**, 814–825.
10 K. Lee, Y. K. Yoo, S. Il Han, J. Lee, D. Lee, C. Kim and J. H. Lee, *Micro nano syst. lett.*, 2017, **5**, 6.
11 A. Krishnamurthy and R. K. Anand, *TrAC, Trends Anal. Chem.*, 2022, **148**, 116537.

12 B. Sabbagh, S. Park and G. Yossifon, *Lab Chip*, 2025, 8–11.

13 S. K. Cho, H. Moon and C. J. Kim, *J. Microelectromech. Syst.*, 2003, **12**, 70–80.

14 D. Chatterjee, H. Shepherd and R. L. Garrell, *Lab Chip*, 2009, **9**, 1219–1229.

15 K. Choi, A. H. C. Ng, R. Fobel and A. R. Wheeler, *Annu. Rev. Anal. Chem.*, 2012, **5**, 413–440.

16 L. Pang, J. Ding, X. X. Liu and S. K. Fan, *TrAC, Trends Anal. Chem.*, 2019, **117**, 291–299.

17 Y. Zhang and Y. Liu, *Biosensors*, 2022, **12**, 1–14.

18 R. P. S. De Campos, D. G. Rackus, R. Shih, C. Zhao, X. Liu and A. R. Wheeler, *Anal. Chem.*, 2019, **91**, 2506–2515.

19 T. H. Lin and D. J. Yao, *J. Adhes. Sci. Technol.*, 2012, **26**, 1789–1804.

20 Y. Liu, P. Jeraldo, H. Mendes-Soares, T. Masters, A. E. Asangba, H. Nelson, R. Patel, N. Chia and M. Walther-Antonio, *ACS Omega*, 2021, **6**, 25642–25651.

21 A. Banerjee, E. Kreit, Y. Liu, J. Heikenfeld and I. Papautsky, *Lab Chip*, 2012, **12**, 758–764.

22 A. Banerjee, J. H. Noh, Y. Liu, P. D. Rack and I. Papautsky, *Micromachines*, 2015, **6**, 172–185.

23 Y. Liu and I. Papautsky, *Micromachines*, 2019, **10**, 1–12.

24 Y. He, Z. Lu, K. Liu, L. Wang, Q. Xu, H. Fan, C. Liu and T. Zhang, *Sens. Actuators, B*, 2024, **399**, 134851.

25 S. C. C. Shih, P. C. Gach, J. Sustarich, B. A. Simmons, P. D. Adams, S. Singh and A. K. Singh, *Lab Chip*, 2015, **15**, 225–236.

26 F. Ahmadi, K. Samlali, P. Q. N. Vo and S. C. C. Shih, *Lab Chip*, 2019, **19**, 524–535.

27 V. A. Papadimitriou, S. A. Kruit, L. I. Segerink and J. C. T. Eijkel, *Lab Chip*, 2020, **20**, 2209–2217.

28 D. T. Phan, Y. Chun and N. T. Nguyen, *RSC Adv.*, 2015, **5**, 44336–44341.

29 M. W. L. Watson, M. J. Jebrail and A. R. Wheeler, *Anal. Chem.*, 2010, **82**, 6680–6686.

30 G. Sathyanarayanan, M. Haapala, C. Dixon, A. R. Wheeler and T. M. Sikanen, *Adv. Mater. Technol.*, 2020, **5**, 1–9.

31 M. Nardecchia, E. Bellini, P. R. Llorca, D. Caprini, N. Lovecchio, G. Petrucci, D. Caputo, G. De Cesare and A. Nascetti, *Procedia Eng.*, 2016, **168**, 1370–1373.

32 S. J. Kim, Y. A. Song and J. Han, *Chem. Soc. Rev.*, 2010, **39**, 912–922.

33 C.-H. Chen, A. Sarkar, Y.-A. Song, M. A. Miller, S. J. Kim, L. G. Griffith, D. A. Lauffenburger and J. Han, *J. Am. Chem. Soc.*, 2011, **133**, 10368–10371.

34 M. Yu, Y. Hou, H. Zhou and S. Yao, *Lab Chip*, 2015, **15**, 1524–1532.

35 B. Sabbagh, N. E. Fraiman, A. Fish and G. Yossifon, *ACS Appl. Mater. Interfaces*, 2023, **15**, 23361–23370.

36 R. Kwak, J. Y. Kang and T. S. Kim, *Anal. Chem.*, 2016, **88**, 988–996.

37 M. Kim, H. Rhee, J. Y. Kang, T. S. Kim and R. Kwak, *J. Visualized Exp.*, 2017, **120**, e55313.

38 D. Velegol, A. Garg, R. Guha, A. Kar and M. Kumar, *Soft Matter*, 2016, **12**, 4686–4703.

39 Z. Petrášek and P. Schwille, *Biophys. J.*, 2008, **94**, 1437–1448.

40 H. Jeon, H. Lee, K. H. Kang and G. Lim, *Sci. Rep.*, 2013, **3**, 1–7.

41 I. Cho, G. Y. Sung and S. J. Kim, *Nanoscale*, 2014, **6**, 4620–4626.

42 A. I. Drygiannakis, A. G. Papathanasiou and A. G. Boudouvis, *Langmuir*, 2009, **25**, 147–152.

43 F. Mugele, A. Klingner, J. Buehrle, D. Steinhauser and S. Herminghaus, *J. Phys.: Condens. Matter*, 2005, **17**, S559.